

Two-Phase Channel Estimation for RIS-Assisted THz Systems with Beam Split

Xin Su, *Student Member, IEEE*, Ruisi He, *Senior Member, IEEE*, Peng Zhang, Bo Ai, *Fellow, IEEE*, Yong Niu, *Member, IEEE* and Gongpu Wang, *Senior Member, IEEE*

Abstract—Reconfigurable intelligent surface (RIS)-assisted terahertz (THz) communication is emerging as a key technology to support ultra-high data rates in future sixth-generation networks. However, the acquisition of accurate channel state information (CSI) in such systems is challenging due to the passive nature of RIS and the hybrid beamforming architecture typically employed in THz systems. To address these challenges, we propose a novel low-complexity two-phase channel estimation scheme for RIS-assisted THz systems with beam split effect. In the proposed scheme, we first estimate the full CSI over a small subset of subcarriers, then extract angular information at both the base station and RIS. Subsequently, we recover the full CSI across remaining subcarriers by determining the corresponding spatial directions and angle-excluded coefficients. Theoretical analysis and simulation results demonstrate that the proposed method achieves superior performance in terms of normalized mean-square error while significantly reducing computational complexity compared to existing algorithms.

Index Terms—Terahertz, beam split, reconfigurable intelligent surface, wideband channel estimation, direction estimation

I. INTRODUCTION

ENVISIONED as a cornerstone technology to meet the requirements of future 6G networks, terahertz (THz) communication holds immense potential for a myriad of applications within the field of the Internet of Things, ranging from intelligent industrial manufacturing to digital twinning technologies and immersive experiences like holographic telepresence and the metaverse [1]–[3]. However, THz communication systems encounter various challenges, including high propagation loss, limited coverage, and susceptibility to atmospheric absorption and scattering [4], [5]. One notable drawback is the severe signal attenuation experienced by transmitted signals, which often necessitate a line-of-sight (LoS) link to maintain communication quality [6]. To address these challenges and unlock the full potential of THz communication, reconfigurable intelligent surface (RIS) has emerged to provide LoS paths by intelligently manipulating the propagation environment [7]. RIS can dynamically adjust reflection properties of a large number of passive reflecting elements to optimize signal transmission and reception [8].

Part of this paper was published at the IEEE VTC 2024 Spring.

X. Su, R. He, P. Zhang, B. Ai and Y. Niu are with the School of Electronics and Information Engineering, Beijing Jiaotong University, Beijing 100044, China (e-mail: 22120124@bjtu.edu.cn; ruisi.he@bjtu.edu.cn; 21120170@bjtu.edu.cn; boai@bjtu.edu.cn; niuy11@163.com).

G. Wang is with the Beijing Key Laboratory of Transportation Data Analysis and Mining, School of Computer and Information Technology, Beijing Jiaotong University, Beijing 100044, China, and also with the China (Wuxi) Institute of Internet of Things, Wuxi 214111, China (e-mail: gp-wang@bjtu.edu.cn).

By strategically controlling the phase shifts of these reflecting elements, RIS can effectively enhance the signal strength, mitigate interference, and improve the overall performance of THz communication systems. However, due to the passive nature of RIS, which lacks signal processing capabilities, the performance enhancement enabled by RIS relies significantly on accurate channel state information (CSI), the acquisition of which can be challenging. Therefore, investigating an efficient channel estimation scheme for RIS-assisted THz communication systems is of great importance.

A. Prior Work

Over the past few years, numerous research works have been dedicated to exploring channel estimation in RIS-assisted high frequency band systems [9]–[14]. Specifically, a sparse representation of RIS-assisted millimeter wave (mmWave) channel has been established, on which compressed sensing based techniques can be implemented for CSI acquisition [9]. In [10], a low-overhead channel estimation method has been proposed based on the double-structure characteristic of RIS-assisted angular cascaded channel. To reduce computational complexity, [11] proposed a non-iterative two-stage framework based on direction-of-arrival (DoA) estimation. The authors in [12] proposed a two-phase channel estimation strategy to reduce pilot overhead. [13] investigated cooperative-beam-training based channel estimation procedure. In [14], a sparse Bayesian learning based channel estimation approach has been developed to compensate the severe off-grid issue.

The above solutions have effectively addressed the channel estimation problem of narrowband systems with utilization of the angular domain sparsity. However, THz communication typically adopts a hybrid beamforming architecture to reduce hardware costs [15]. When considering this architecture, the beam split effect becomes inevitable. This effect occurs due to the wider bandwidth of THz signals and the enormous number of RIS elements, which causes path components to split into distinct spatial directions at different subcarrier frequencies [16]. This phenomenon leads to a considerable degradation in achievable data rates, which counteracts the benefits of RIS-assisted THz systems.

To address this issue, beam split effect in RIS-assisted THz systems has been investigated in [17]–[19]. In particular, [17] introduced a beam-split-aware orthogonal matching pursuit (BSA-OMP) approach to automatically mitigate beam split. In [18], a low-complexity beam squint mitigation scheme is proposed based on generalized-OMP estimator. The au-

thors in [19] proposed a robust regularized sensing-beam-split-OMP-based scheme to estimate beam split affected RIS-assisted cascaded channel. These works primarily focus on mitigating beam split effects within the context of cascaded channels using well-designed dictionaries covering the entire beamspace. However, an alternative approach is to focus on the physical directions of the channel components to reduce computational complexity [20]–[22]. Specifically, the authors in [20] regarded channel estimation problem as a block-sparse recovery problem. [21] proposed a beam split pattern detection based wideband channel estimation scheme where the physical DoAs are prioritized for determination. In [22], a three-stage wideband channel estimation scheme is proposed where angle-of-arrivals (AoAs) and angle-of-departure (AoDs) are determined and refined to reconstruct the wideband channel with beam split effect. Although these algorithms achieve accurate channel estimation, they require execution at each SC or simultaneous processing of all SCs, which may introduce additional unaffordable computations. Moreover, the passive nature of RIS complicates the precise acquisition of angles at the RIS, which often results in the availability of only coupled angles. Therefore, this motivates the development of a low-complexity channel estimation scheme in RIS-assisted wideband THz systems with beam split effect.

B. Main Contributions

To address the issue discussed above, we presented some preliminary results on estimating the RIS-assisted cascaded channel [23]. In this paper, we significantly expand on the previous work and propose a two-phase efficient channel estimation scheme for RIS-assisted wideband THz systems with beam split. Our main contributions are summarized as follows:

- We propose a novel low-complexity channel estimation protocol for general RIS-assisted wideband THz communication scenarios with beam split effect, as depicted in Fig. 1. The channel estimation scheme is divided into two phases: full CSI estimation for two SCs in Phase I and remaining SCs estimation in Phase II. By employing information from only two SCs, this protocol can significantly reduce the computational complexity while maintaining complete and accurate channel estimation.
- In Phase I, we propose a two-step method to acquire full CSI for the selected two SCs. Specifically, in Step 1, we propose a simplified cyclic beam split (CBS) dictionary to reduce the size from the scale of Q^2 to a linear scale of Q . Using this dictionary, we reformulate the problem as a generalized sparse recovery problem. Moreover, we discuss the selection of different sparse recovery algorithms. In Step 2, we first design a heuristic DoD estimation method at BS according to the estimated cascaded channel obtained in Step 1. We then reformulate the coupled angles at RIS as a typical DoA estimation problem and design a double sensing-multiple signal classification (DS-MUSIC) algorithm by integrating the angular information from the two selected SCs. We also provide insights into the selection of two SCs. In Phase II, given angular information from Phase I, we employ

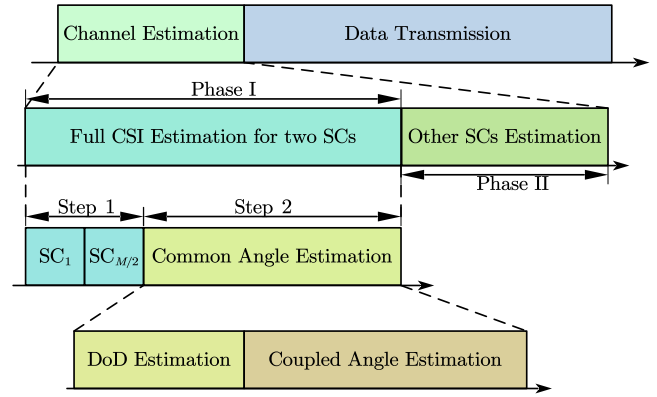


Fig. 1. Two-phase channel estimation protocol and frame structure.

a simple least squares (LS) algorithm to estimate the channels for the remaining SCs.

- Through the analysis of algorithm complexity, our proposed protocol significantly reduces the computational complexity compared to the existing sparse recovery solutions. Additionally, numerical results demonstrate that the NMSE performance of our proposed channel estimation scheme closely approaches that of oracle-LS method. By focusing on a two-step estimation process for two SCs and applying a simplified LS algorithm for the remaining SCs, the proposed method can achieve both reduction of computational complexity and acquisition of accurate CSI.

The remainder of this paper is organized as follows. In Section II, we first describe the RIS-assisted wideband THz communication setup and the beam split effect. In Section III, we describe our proposed channel estimation protocol. Section V provides an analysis of the computational complexity of our proposed scheme, with a comparison to existing methods. Finally, we conclude the paper in Section VI.

Notations: Boldface lower-case and capital letters represent column vectors and matrices, respectively. $(\cdot)^*$, $(\cdot)^\dagger$, $(\cdot)^H$ and $(\cdot)^\ddagger$ denote conjugate, transpose, transpose-conjugate and pseudo-inverse operation, respectively. \mathbb{E} and Var represent statistical expectation and variance, respectively. \mathbb{N} , \mathbb{C} and \mathbb{R} denote the set of integers, complex numbers and real numbers, respectively. \mathbf{I}_N is $N \times N$ size identity matrix and tr is the trace. \otimes denote Kronecker product, $*$ and \bullet denote Khatri-Rao product and transposed Khatri-Rao product, respectively.

II. SYSTEM AND CHANNEL MODEL

A. Signal and Channel Model

We consider a RIS-assisted wideband THz MIMO system employing hybrid beamforming architecture that integrates both analog and baseband processing, as depicted in Fig. 2. Assuming that the BS equipped with N_T antennas and N_{RF} (where $N_{RF} < N_T$) RF chains is deployed to serve K single-antenna UEs. The RIS employs a uniform linear array (ULA) comprised of N_R reflecting elements, which is manipulated by a smart controller operated by the BS. Besides, the OFDM

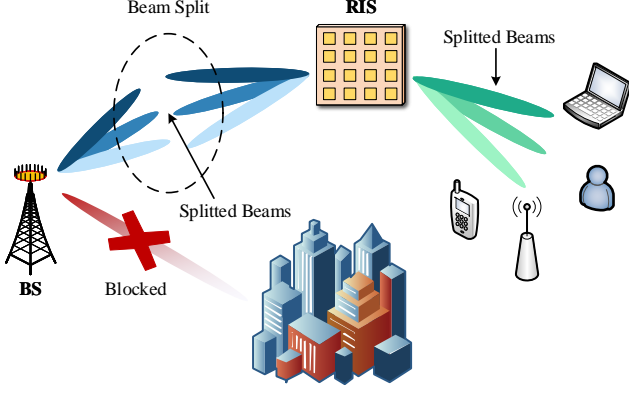


Fig. 2. RIS-assisted THz communication system with beam split effect.

system is considered with M subcarriers, central frequency f_c and bandwidth B .

In this paper, we assume that the channel is quasi-static, i.e., the channel remains approximately constant in a channel coherence block with D subframes [12]. For each coherence block, channel estimation is firstly performed during T subframes, and downlink data transmission is then carried out during the remaining $D - T$ subframes. Moreover, each subframe of the downlink channel estimation period is divided into P time slots, with P baseband beamformers operating alternatively across different time slots. Additionally, we assume that the direct BS-UE links are blocked by obstacles [20]. Therefore, we mainly focus on the downlink channel estimation of the cascaded BS-RIS-UE channel.

As a cost-performance trade-off, hybrid beamforming architecture is typically employed in THz MIMO systems [15]. In our considered system, we assume that P frequency-dependent baseband beamformers $\mathbf{W}_t^{\text{BB}}[m] = [\mathbf{w}_{t,1}^{\text{BB}}[m], \dots, \mathbf{w}_{t,P}^{\text{BB}}[m]] \in \mathbb{C}^{N_{\text{RF}} \times P}$ are employed to process P orthogonal pilot signals $\mathbf{S}_t \triangleq \text{Diag}\{s_{t,1}, \dots, s_{t,P}\} \in \mathbb{C}^{P \times P}$ per time slot. Meanwhile, a frequency-independent analog beamformer $\mathbf{W}^{\text{RF}} \in \mathbb{C}^{N_{\text{T}} \times N_{\text{RF}}}$ is employed to achieve gain improvement in the direction of RIS with each entry is subject to the unit-modulus constraint, i.e., $|\mathbf{W}^{\text{RF}}_{i,j}| = 1/\sqrt{N_{\text{T}}}$ for $i = 1, \dots, N_{\text{T}}$ and $j = 1, \dots, N_{\text{RF}}$. We assume that the analog beamformer remains unchanged over multiple channel coherence blocks due to the relatively static nature of the RIS physical location compared to the dynamic channel coefficients. Therefore, we define $\mathbf{W}_t[m] \triangleq \mathbf{W}^{\text{RF}} \mathbf{W}_t^{\text{BB}}[m] \in \mathbb{C}^{N_{\text{T}} \times P}$ as the hybrid beamformer which consists of P beamformer vectors, i.e., $\mathbf{W}_t[m] = [\mathbf{w}_{t,1}[m], \dots, \mathbf{w}_{t,P}[m]]$. Let $\mathbf{G}[m] \in \mathbb{C}^{N_{\text{R}} \times N_{\text{T}}}$ and $\mathbf{h}_k[m] \in \mathbb{C}^{N_{\text{R}}}$ denote the channel from BS to RIS and RIS to k -th UE at the m -th SC, respectively. At time slot p of subframe t , the received measurement $y_{k,t,p}[m]$ by k -th UE at the m -th SC can be expressed as

$$y_{k,t,p}[m] = \mathbf{h}_k[m] \text{Diag}(\boldsymbol{\theta}_t) \mathbf{G}[m] \mathbf{w}_{t,p}[m] s_{t,p}[m] + n_{k,t,p}[m] \\ = \boldsymbol{\theta}_t \text{Diag}(\mathbf{h}_k[m]) \mathbf{G}[m] \mathbf{w}_{t,p}[m] s_{t,p}[m] + n_{k,t,p}[m], \quad (1)$$

where $n_{k,t,p}[m] \sim \mathcal{CN}(0, 2\varepsilon)$ is the complex additive white Gaussian noise (AWGN). Besides, $\boldsymbol{\theta}_t = [e^{j\theta_{t,1}}, \dots, e^{j\theta_{t,N_{\text{R}}}}]$

is the phase-shift matrix of RIS at subframe t with a constant reflection amplitude constraint [24].

Let $\mathbf{r}_{t,p}[m] \triangleq \mathbf{w}_{t,p}[m] s_{t,p}[m] \in \mathbb{C}^{N_{\text{T}}}$ denote the processed transmitted signal and combining the processed signals during P successive time slots $\mathbf{R}_t[m] \triangleq [\mathbf{r}_{t,1}[m], \dots, \mathbf{r}_{t,P}[m]] \in \mathbb{C}^{N_{\text{T}} \times P}$, the combined measurement vector $\tilde{\mathbf{y}}_{k,t}[m] \in \mathbb{C}^{1 \times P}$ is expressed as

$$\tilde{\mathbf{y}}_{k,t}[m] = \boldsymbol{\theta}_t \text{Diag}(\mathbf{h}_k[m]) \mathbf{G}[m] \mathbf{R}_t[m] + \tilde{\mathbf{n}}_{k,t}[m], \quad (2)$$

where $\tilde{\mathbf{n}}_{k,t}[m] \triangleq [n_{k,t,1}[m], \dots, n_{k,t,P}[m]] \in \mathbb{C}^{1 \times P}$ denotes the combined AWGN. Therefore, the cascaded channels can be expressed as [25]

$$\mathbf{H}_k^{\text{cas}}[m] = \text{Diag}(\mathbf{h}_k[m]) \mathbf{G}[m] \in \mathbb{C}^{N_{\text{R}} \times N_{\text{T}}}. \quad (3)$$

We adopt the widely used Saleh-Valenzuela channel model for both BS-RIS channel and RIS-UE channel [26]. The BS-RIS channel $\mathbf{G}[m]$ at the m -th SC is expressed as

$$\mathbf{G}[m] = \sum_{l=1}^L \alpha_l \mathbf{a}_{\text{R},m}(\tilde{\psi}_l) \mathbf{a}_{\text{T},m}^{\text{H}}(\tilde{\varphi}_l) e^{-j2\pi\tau_l f_m}, \quad (4)$$

where L represents the number of propagation paths between BS and RIS, α_l , τ_l , $\tilde{\psi}_l$ and $\tilde{\varphi}_l$ represent the complex gain, the time delay, the physical angle-of-departure (AoD) at BS and angle-of-arrival (AoA) at RIS for the l -th path, respectively. Besides, f_m denotes the frequency of the m -th SC, which is given by

$$f_m = f_c + \frac{B}{M} \left(m - 1 - \frac{M-1}{2} \right), \forall m = 1, 2, \dots, M, \quad (5)$$

where f_c is the central carrier frequency. Besides, $\mathbf{a}_{\text{T},m} \in \mathbb{C}^{N_{\text{T}}}$ and $\mathbf{a}_{\text{R},m} \in \mathbb{C}^{N_{\text{R}}}$ are the normalized array response vectors (ARVs) associated with BS and RIS, respectively, given by

$$\mathbf{a}_{\text{T},m}(\tilde{u}) \triangleq \frac{1}{\sqrt{N_{\text{T}}}} e^{-j2\pi \sin(\tilde{u}) \mathbf{n}_t d_{\text{BS}} / \lambda_m}, \quad (6a)$$

$$\mathbf{a}_{\text{R},m}(\tilde{v}) \triangleq \frac{1}{\sqrt{N_{\text{R}}}} e^{-j2\pi \sin(\tilde{v}) \mathbf{n}_r d^{\text{RIS}} / \lambda_m}, \quad (6b)$$

where $\lambda_m = c/f_m$ is the wavelength of the m -th subcarrier. d_{BS} and d^{RIS} denote the antenna spacing of BS and RIS, respectively. Besides, $\mathbf{n}_t = [0, 1, \dots, N_{\text{T}} - 1]$ and $\mathbf{n}_r = [0, 1, \dots, N_{\text{R}} - 1]$, respectively. By defining the angle vectors $\tilde{\boldsymbol{\psi}} = [\tilde{\psi}_1, \dots, \tilde{\psi}_L]$ and $\tilde{\boldsymbol{\varphi}} = [\tilde{\varphi}_1, \dots, \tilde{\varphi}_L]$, $\mathbf{G}[m]$ can be transformed into the virtual angular representation (VAD) form as

$$\mathbf{G}[m] = \mathbf{A}_{\text{R},m}(\tilde{\boldsymbol{\psi}}) \boldsymbol{\Sigma}_m \mathbf{A}_{\text{T},m}^{\text{H}}(\tilde{\boldsymbol{\varphi}}), \quad (7)$$

where $\mathbf{A}_{\text{R},m}(\tilde{\boldsymbol{\psi}}) = [\mathbf{a}_{\text{R},m}(\tilde{\psi}_1), \dots, \mathbf{a}_{\text{R},m}(\tilde{\psi}_L)]$ and $\mathbf{A}_{\text{T},m}(\tilde{\boldsymbol{\varphi}}) = [\mathbf{a}_{\text{T},m}(\tilde{\varphi}_1), \dots, \mathbf{a}_{\text{T},m}(\tilde{\varphi}_L)]$ denote the array response matrix (ARM) of the AoDs at BS and AoAs at RIS, respectively. $\boldsymbol{\Sigma}_m = \text{Diag}(\alpha_1 e^{-j2\pi\tau_1 f_m}, \dots, \alpha_L e^{-j2\pi\tau_L f_m})$ is the angle-excluded matrix. Similarly, the channel $\mathbf{h}_k[m] \in \mathbb{C}^{1 \times N_{\text{R}}}$ between RIS and UE- k at the m -th SC can be formulated as

$$\mathbf{h}_k[m] = \sum_{j=1}^{J_k} \beta_{k,j} \mathbf{a}_{\text{R},m}^{\text{H}}(\tilde{\vartheta}_{k,j}) e^{-j2\pi\mu_{k,j} f_m}, \quad (8)$$

where J_k represents the number of propagation paths between RIS and UE- k , $\beta_{k,j}$, $\mu_{k,j}$ and $\tilde{\vartheta}_{k,j}$ represent the complex gain, the time delay and the AoD at RIS for the j -th path, respectively. By defining $\tilde{\boldsymbol{\vartheta}}_k = [\tilde{\vartheta}_{k,1}, \dots, \tilde{\vartheta}_{k,J_k}]$, we transform $\mathbf{h}_k[m]$ into the VAD form as

$$\mathbf{h}_k[m] = \boldsymbol{\beta}_{k,m}^T \mathbf{A}_{R,m}^H(\tilde{\boldsymbol{\vartheta}}_k), \quad (9)$$

where $\boldsymbol{\beta}_{k,m} = [\beta_{k,1} e^{-j2\pi\mu_{k,1}f_m}, \dots, \beta_{k,J_k} e^{-j2\pi\mu_{k,J_k}f_m}]^T$ is the angle-excluded vector for the k -th UE. $\mathbf{A}_{R,m}(\tilde{\boldsymbol{\vartheta}}_k) = [\mathbf{a}_{R,m}(\tilde{\vartheta}_{k,1}), \dots, \mathbf{a}_{R,m}(\tilde{\vartheta}_{k,J_k})]$ denotes the ARM of the AoDs at RIS. Substituting (7) and (9) into (3), the cascaded channel $\mathbf{H}_k^{\text{cas}}[m]$ can be rewritten as

$$\begin{aligned} \mathbf{H}_k^{\text{cas}}[m] &= \text{Diag}(\boldsymbol{\beta}_{k,m}^T \mathbf{A}_{R,m}^H(\tilde{\boldsymbol{\vartheta}}_k)) \mathbf{A}_{R,m}(\tilde{\boldsymbol{\psi}}) \boldsymbol{\Sigma}_m \mathbf{A}_{T,m}^H(\tilde{\boldsymbol{\varphi}}) \\ &= (\mathbf{A}_{R,m}^*(\tilde{\boldsymbol{\vartheta}}_k) \boldsymbol{\beta}_{k,m}) \bullet (\mathbf{A}_{R,m}(\tilde{\boldsymbol{\psi}}) \boldsymbol{\Sigma}_m \mathbf{A}_{T,m}^H(\tilde{\boldsymbol{\varphi}})) \\ &= (\mathbf{A}_{R,m}^*(\tilde{\boldsymbol{\vartheta}}_k) \bullet \mathbf{A}_{R,m}(\tilde{\boldsymbol{\psi}})) (\boldsymbol{\beta}_{k,m} \otimes \boldsymbol{\Sigma}_m) \mathbf{A}_{T,m}^H(\tilde{\boldsymbol{\varphi}}). \end{aligned} \quad (10)$$

B. Beam Split Effect

According to (4) and (8), THz channel varies across different SCs due to the beam split effect¹. This phenomenon is caused by the ultra-wide bandwidth and extensive antenna arrays and reflecting elements in RIS-assisted wideband THz systems. Beams generated by the frequency-independent analog beamforming vector and then reflected by the frequency-independent RIS phase shift matrix would split into totally distinct spatial directions. Typically, antenna spacings are set to half the wavelength at the central frequency f_c , i.e., $d_{\text{BS}} = d_{\text{RIS}} = \lambda_c/2$, where $\lambda_c = c/f_c$ is the wavelength of the central frequency [28]. For simplicity, we define the variables $u \triangleq \sin \tilde{u} \in [-1, 1]$ and $v \triangleq \sin \tilde{v} \in [-1, 1]$ to represent the physical directions. Substituting the half-wavelength configuration into (6a) and (6b), the ARVs can be rewritten as

$$\mathbf{a}_{T,m}(u) = \frac{1}{\sqrt{N_T}} e^{-j\pi\eta_m u n_t}, \quad (11a)$$

$$\mathbf{a}_{R,m}(v) = \frac{1}{\sqrt{N_R}} e^{-j\pi\eta_m v n_r}, \quad (11b)$$

where $\eta_m \triangleq f_m/f_c$ represents the relative frequency. As shown in (11), the spatial directions can be represented by

$$u_m = \eta_m u, \quad (12a)$$

$$v_m = \eta_m v. \quad (12b)$$

In the lower frequency bands such as mmWave, the subcarrier frequencies are relatively closer, which causes slight beam squint with $\eta_m \approx 1$ which means that the ARVs at all SC frequencies are almost identical [20], [28]. However, due to the ultra large bandwidth in THz band, η_m deviates significantly from one. Therefore, the difference between physical directions and spatial directions becomes significant and cannot be ignored.

¹The beam split effect can be seen as a severe version of beam squint effect in mmWave band [27].

In wideband RIS-assisted THz systems, beam split effect occurs at both BS and RIS, which leads to severe performance degradation in channel estimation algorithms [27]. Therefore, it is crucial to develop an effective channel estimation scheme to acquire accurate CSI under beam split effect.

III. CHANNEL ESTIMATION

A. Channel Estimation Protocol

Traditional channel estimation algorithms require significant redesign of the codebook, as conventional dictionaries fail to cover additional angle information introduced by beam split effect [17]. This additional angle information will complicate the design of dictionaries. Furthermore, the beam split effect disperses the channel for each subcarrier into different spatial directions, which requires well-designed channel estimation algorithms to operate on each subcarrier individually, which can significantly increase computational complexity.

To address these challenges, we propose a novel low-complexity channel estimation protocol, which is divided into two main phases, as depicted in Fig. 1. The first phase, which is the most challenging aspect of the protocol, mainly focuses on estimating the full CSI for two selected subcarriers, which includes estimation of cascaded channel, the AoDs at BS, and the coupled angles at RIS. Due to its complexity, we further divide this phase into two steps. In Step 1, we employ sparse recovery algorithms to estimate the cascaded channel for the two subcarriers. In Step 2, we focus on heuristic algorithms for common angles estimation. Given the full CSI estimation from the first phase, we then employ a simple LS algorithm to estimate the channels for the remaining subcarriers.

B. Cascaded Channel Estimation

In this subsection, we focus on the estimation of cascaded channel for one specific subcarrier. In the following steps, we first present the angular domain sparse representation in RIS-assisted THz channels. Then, we introduce the simplified dictionary, i.e., CBS dictionary. Based on this simplified dictionary, we reformulate the channel estimation problem as a sparse recovery problem. Finally, we provide a detailed analysis of existing sparse recovery algorithms.

1) *Angular Domain Sparse Representation*: The sparse angular domain representation of the cascaded channel $\mathbf{H}_k^{\text{cas}}[m]$ is given by

$$\mathbf{H}_k^{\text{cas}}[m] = \tilde{\boldsymbol{\Xi}}_{R,m} (\tilde{\boldsymbol{\beta}}_{k,m} \otimes \tilde{\boldsymbol{\Sigma}}_m) \mathbf{C}_{T,m}^H, \quad (13)$$

where $\tilde{\boldsymbol{\Xi}}_{R,m} \triangleq \mathbf{C}_{R,m}^* \bullet \mathbf{C}_{R,m} \in \mathbb{C}^{N_R \times Q_R^2}$ is the coupled dictionary, $\tilde{\boldsymbol{\Sigma}}_m \in \mathbb{C}^{Q_R \times Q_T}$ and $\tilde{\boldsymbol{\beta}}_{k,m} \in \mathbb{C}^{Q_R}$ are the sparse formulation with L and J_k non-zero entries corresponding to the angle-excluded matrix of BS-RIS channel and the angle-excluded vector of RIS-UE channel, respectively. Additionally, the overcomplete dictionaries of the BS and RIS directions can be expressed as

$$\mathbf{C}_{T,m} = [\mathbf{a}_{T,m}(\tilde{\vartheta}_1), \dots, \mathbf{a}_{T,m}(\tilde{\vartheta}_{Q_T})], \quad (14a)$$

$$\mathbf{C}_{R,m} = [\mathbf{a}_{R,m}(\tilde{\vartheta}_1), \dots, \mathbf{a}_{R,m}(\tilde{\vartheta}_{Q_R})], \quad (14b)$$

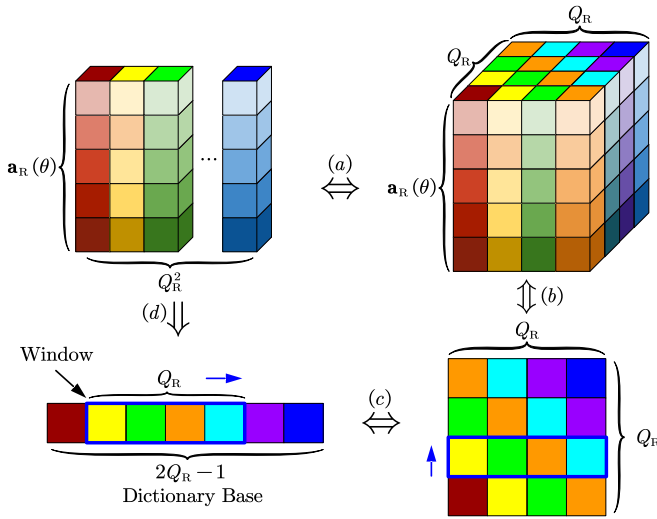


Fig. 3. Coupled dictionary simplification diagram.

where $Q_T \gg N_T$ and $Q_R \gg N_R$ are the quantization level of the BS and RIS directions, respectively. Moreover, $\bar{v}_q = \delta \cdot q - (Q + 1)/Q$ with $Q \in \{Q_T, Q_R\}$ denotes the spatial direction sample, $\delta = 2/Q$ is the interval between two adjacent samples.

2) *Simplified Dictionary*: Note that the coupled dictionary $\tilde{\Xi}_{R,m}$ in (13) is derived from the transposed Khatri-Rao product, which contains a significant number of redundant columns due to the fixed sampling intervals. For narrowband channel model, this will result in only Q_R unique columns which are exactly the first Q_R columns [9]. However, for wideband THz channel with beam split effect, this simplification is no longer suitable due to the frequency-dependent nature of the ARVs.

Proposition 1. *The number of unique columns of dictionary $\tilde{\Xi}_{R,m}$ is $Q_B = 2Q_R - 1$, and the coupled dictionary can be simplified by including only the first and the last Q_R columns of the coupled dictionary $\tilde{\Xi}_{R,m}$, which can be given as*

$$\Xi_{R,m} \triangleq [\tilde{\Xi}_{R,m}(Q_R^2 - Q_R + 1 : Q_R^2); \tilde{\Xi}_{R,m}(2 : Q_R)], \quad (15)$$

where $\Xi_{R,m} \in \mathbb{C}^{N_R \times Q_B}$ is the simplified dictionary.

Proof. We first define the parameter sequence $\bar{v}_{q_1} = \delta \cdot q_1 - (Q + 1)/Q, \forall q_1 = 1, \dots, Q_R$ which corresponds one-to-one with Q_R ARV columns in the dictionary $\mathbf{C}_{R,m}$. Similarly, we define the sequence $\bar{v}_{q_2} = -\delta \cdot q_2 + (Q + 1)/Q$ to correspond to Q_R ARV columns in the conjugate dictionary $\mathbf{C}_{R,m}^*$. Thus, the column vectors of $\mathbf{C}_{R,m}^* \bullet \mathbf{C}_{R,m}$ can be expressed as $\mathbf{a}_{R,m}(\bar{v}_{q_1} - \bar{v}_{q_2})$ for $q_1, q_2 = 1, \dots, Q_R$. The j -th column of the coupled dictionary $\tilde{\xi}_{R,m,j}$ can be expressed as

$$\tilde{\xi}_{R,m,j} = \mathbf{a}_{R,m}(\delta(q_1 - q_2)), \quad (16)$$

where $j = (q_2 - 1)Q_R + q_1, \forall q_1, q_2 = 1, \dots, Q_R$. Based on the fact that $q_1 - q_2 \in [1 - Q_R, Q_R - 1]$, the number of unique columns of coupled dictionary $\tilde{\Xi}_{R,m}$ is $Q_B = 2Q_R - 1$.

Then, we simplify the coupled dictionary $\tilde{\Xi}_{R,m}$ step by step from (a) to (d) as shown in Fig. 3. As depicted in step (a), we

reshape the overcomplete dictionary $\tilde{\Xi}_{R,m}$ of length Q_R^2 ARV columns into a three-dimensional matrix where each column represents an ARV. Given that ARV vectors can be uniquely determined by known angles in (16), we use the sequences $q_1, q_2 = 1, \dots, Q_R$ to index the corresponding ARV columns. In step (b), we form the index matrix $\mathbf{Q} \in \mathbb{N}^{Q_R \times Q_R}$ with elements $[\mathbf{Q}]_{i,j} = q_1(i) - q_2(j)$ for $i, j = 1, \dots, Q_R$. It is noticed that due to the cyclic shift property of this dictionary, the dictionary base can be represented entirely by combining just the first and last rows. This means that we can reconstruct the original dictionary $\tilde{\Xi}_{R,m}$ with a sliding window of length Q_R . Therefore, the simplified CBS dictionary $\Xi_{R,m}$ can be given as in (15). Moreover, substituting $q_2 = Q_R$ into (16), the q -th column where $q = 1, \dots, Q_B$ of $\Xi_{R,m}$ can be formulated as

$$\xi_{R,m,q} = \mathbf{a}_{R,m} \left(2 \frac{q - Q_R}{Q_R} \right). \quad (17)$$

3) *Sparse Recovery Reformulation*: By substituting the simplified CBS dictionary $\Xi_{R,m}$ into (13), the RIS-assisted cascaded channel can be rewritten as

$$\mathbf{H}_k^{\text{cas}}[m] = \Xi_{R,m} \mathbf{X}_{k,m} \mathbf{C}_{T,m}^H, \quad (18)$$

where $\mathbf{X}_{k,m} \in \mathbb{C}^{Q_B \times Q_T}$ is the total angle-excluded matrix, each row of $\mathbf{X}_{k,m}$ is a superposition of row subsets in $\tilde{\mathbf{X}}_{k,m} \triangleq \tilde{\beta}_{k,m} \otimes \tilde{\Sigma}_m$, i.e., $\mathbf{X}_{k,m}(i, :) = \sum_{j \in \mathcal{P}_i} \tilde{\mathbf{X}}_{k,m}(j, :)$. \mathcal{P}_i denotes the set of indices associated with the columns in $\tilde{\Xi}_{R,m}$ that match the i -th column of $\Xi_{R,m}$. Therefore, there are at most $L_{\text{tot},k} = L \times J_k$ nonzero entries in $\mathbf{X}_{k,m}$. Employing the Kronecker product property, the vectorized RIS-assisted cascaded channel $\mathbf{h}_k^{\text{cas}}[m] \in \mathbb{C}^{N_T N_R \times Q_B Q_T}$ can be given by

$$\mathbf{h}_k^{\text{cas}}[m] = \mathbf{\Pi}_m \mathbf{x}_{k,m}, \quad (19)$$

where $\mathbf{x}_{k,m} = \mathbf{X}_{k,m}(:, :) \in \mathbb{C}^{Q_B Q_T}$ represents $\mathbf{X}_{k,m}$ in vector form, $\mathbf{\Pi}_m \triangleq (\mathbf{C}_{T,m}^* \otimes \Xi_{R,m}) \in \mathbb{C}^{N_T N_R \times Q_B Q_T}$ denotes the total dictionary.

By substituting (19) into (2) and vectorizing, the sparse system formulation can be expressed as

$$\mathbf{y}_{k,t}[m] = (\mathbf{R}_t^T[m] \otimes \boldsymbol{\theta}_t) \mathbf{\Pi}_m \mathbf{x}_{k,m} + \mathbf{n}_{k,t}[m], \quad (20)$$

where $\mathbf{y}_{k,t}[m] \in \mathbb{C}^P$ is the vector form of $\tilde{\mathbf{y}}_{k,t}[m]$. Stacking the measurement vectors collected at T successive subframes $\mathbf{y}_k[m] = [\mathbf{y}_{k,1}^T[m], \dots, \mathbf{y}_{k,T}^T[m]]^T \in \mathbb{C}^{PT}$, the received signal can be expressed as

$$\mathbf{y}_k[m] = \mathbf{\Psi}_m \mathbf{x}_{k,m} + \mathbf{n}_k[m], \quad (21)$$

where $\mathbf{\Psi}_m = \bar{\mathbf{R}}_m \mathbf{\Pi}_m$ and

$$\bar{\mathbf{R}}_m \triangleq \begin{bmatrix} \mathbf{R}_1^T[m] \otimes \boldsymbol{\theta}_1 \\ \vdots \\ \mathbf{R}_T^T[m] \otimes \boldsymbol{\theta}_T \end{bmatrix}. \quad (22)$$

Note that the observation matrix $\mathbf{\Psi}_m \in \mathbb{C}^{PT \times Q_B Q_T}$ is a sparse matrix. To map this problem to the real number domain for

resolution, we then transform the complex form in (21) to the equivalent real form

$$\begin{bmatrix} \Re\{\mathbf{y}_k[m]\} \\ \Im\{\mathbf{y}_k[m]\} \end{bmatrix} = \begin{bmatrix} \Re\{\Psi_m\} & -\Im\{\Psi_m\} \\ \Im\{\Psi_m\} & \Re\{\Psi_m\} \end{bmatrix} \begin{bmatrix} \Re\{\mathbf{x}_{k,m}\} \\ \Im\{\mathbf{x}_{k,m}\} \end{bmatrix} + \begin{bmatrix} \Re\{\mathbf{n}_k[m]\} \\ \Im\{\mathbf{n}_k[m]\} \end{bmatrix}, \quad (23)$$

By systematically assigning symbols to each matrix in (23), the sparse recovery problem can be reformulated as

$$\mathbf{y} = \Psi \mathbf{x} + \mathbf{n}. \quad (24)$$

For simplicity, we use a simplified subscript notation by omitting the index for the matrices and vectors. By defining $T_{\text{tot}} \triangleq PT$ and $Q_{\text{tot}} \triangleq Q_B Q_T$, let $\mathbf{y} \in \mathbb{C}^{T_{\text{tot}}}$ denote the measurement vector, $\Psi \in \mathbb{C}^{T_{\text{tot}} \times Q_{\text{tot}}}$ denote the observation matrix and $\mathbf{x} \in \mathbb{C}^{Q_{\text{tot}}}$ denote the sparse representation vector to be estimated with sparsity L_{tot} .

4) *Sparse Recovery Algorithm Analysis*: In designing our channel estimation algorithm, the selection of an appropriate sparse recovery algorithm is crucial due to the unique sparsity characteristics of RIS-assisted THz channels. We considered LS, OMP, and GAMP for this purpose.

a) LS: The LS algorithm, while straightforward, solves the sparse recovery problem by minimizing the residual sum of squares. However, its computational complexity, which is $\mathcal{O}(Q_{\text{tot}}^3)$, will become significantly high for large matrix dimensions. Consequently, LS is not practical for the initial full CSI estimation phase due to its high computational demands.

b) OMP: OMP is a widely used greedy algorithm that reconstructs the signal by iteratively selecting the dictionary atoms that best match the current residual. The computational complexity of OMP is $\mathcal{O}(L_{\text{tot}} Q_{\text{tot}}^2)$, which is relatively efficient. However, OMP has a nature of ‘‘hard estimation’’, which means that it makes definitive decisions at each step without retaining detailed probabilistic information about the signal. This approach can lead to suboptimal performance, particularly in noisy environments or with complex signal structures.

c) GAMP: In contrast to OMP, GAMP uses a probabilistic approach within a message-passing framework to perform global updates, which will maintain a distribution of possible values for each signal element. The computational complexity of GAMP is $\mathcal{O}(Q_{\text{tot}}^2)$ which is similar to OMP but involves more sophisticated probabilistic calculations. GAMP’s ‘‘soft estimation’’ process retains probabilistic information throughout the iterations, which leads to more accurate estimation. This makes GAMP particularly advantageous in environments with high noise levels or complex signals.

Despite the similar computational complexity of GAMP and OMP, GAMP’s superior accuracy and robustness make it the preferred choice for initial full CSI estimation². Additionally, due to the probabilistic model employed by the ‘‘soft estimation’’ process, GAMP can ensure more reliable angular information determination and avoid the errors caused by ‘‘hard estimation’’.

Moreover, for the final stage of channel estimation involving the remaining subcarriers, we employ the LS algorithm. The

²Detailed investigation of CBS-based GAMP scheme has been discussed in our previous work [19]

angular information obtained from the initial estimation phase significantly reduces the dictionary matrix dimensions, which will make LS computationally feasible and effective. This stage can benefit more from the simplicity and accuracy of LS method.

C. Common Angle Estimation

In this subsection, we focus on the estimation of common angles. Using the selected GAMP algorithm from Section III-B, we can obtain the sparse signal vector \mathbf{x} , denoted as $\hat{\mathbf{x}}_{k,m} = [x_1, \dots, x_{Q_{\text{tot}}}]^T$. By substituting $\hat{\mathbf{x}}_{k,m}$ into (19), the estimated cascaded channel can be expressed as

$$\hat{\mathbf{h}}_k^{\text{cas}}[m] = \mathbf{\Pi}_m \hat{\mathbf{x}}_{k,m}. \quad (25)$$

This method implies that we could perform the estimation for each subcarrier independently to obtain the channel estimates for all subcarriers. However, this requires implementing the estimation algorithm M times, which would result in an unacceptably high computational complexity. While the beam split effect complicates the channel estimation process, it also offers some insights. It is noticed in (11) that different subcarriers share common physical directions, with the only different term η_m . This indicates that the physical angles remain constant across different subcarriers. Inspired by this, we perform the cascaded channel estimation on only a small subset of subcarriers to acquire the common physical angles. We select $\hat{\mathbf{h}}_k^{\text{cas}}[m]$ for $m \in \{1, M/2\}$. Given this estimation, we can further estimate the common directions, i.e., the DoDs at the BS and the coupled directions at the RIS.

1) *Common DoDs Estimation at BS*: Given the estimated cascaded channel $\hat{\mathbf{h}}_k^{\text{cas}}[m] = \mathbf{\Pi}_m \hat{\mathbf{x}}_{k,m}$, $\bar{m} \in \{1, M/2\}$, it is noticed that the q -th ($q = 1, \dots, Q_{\text{tot}}$) entry in $\hat{\mathbf{x}}_{k,\bar{m}}$ corresponds to the q -th column in $\mathbf{\Pi}_{\bar{m}}(:, q)$. This means that given the accurate estimation of $\hat{\mathbf{x}}$, we only need to determine its non-zero positions corresponding to the columns in the matrix $\mathbf{\Pi}_{\bar{m}}$. Since $\mathbf{\Pi}_{\bar{m}} \triangleq (\mathbf{C}_{T,\bar{m}}^* \otimes \mathbf{\Xi}_{R,\bar{m}})$ is in one-to-one correspondence with the ARVs, this relationship allows us to directly obtain the DoDs at BS. However, inevitable noise and estimation errors can cause power leakage in the estimated $\hat{\mathbf{x}}_{k,\bar{m}}$, which will lead to more than Σ_k non-zero entries. To address this, we propose a heuristic method to determine the accurate non-zero positions, referred to as common physical support, and calculate the corresponding physical DoDs at the BS, as summarized in Algorithm 1.

In the proposed method, we first establish the normalized energy basis vector $\tilde{\epsilon}_{\bar{m}}$, where each entry is the normalized value of the corresponding element in $\hat{\mathbf{x}}_{k,\bar{m}}$ (Step 2). As observed in Section III-B3, $\mathbf{\Pi}_{\bar{m}}$ can be regarded as a block matrix of Q_T blocks, each containing Q_B columns. Since each block in $\mathbf{\Pi}_{\bar{m}}$ is aligned with a physical DoD at BS, $\tilde{\epsilon}_{\bar{m}}$ can be partitioned in the same way. By accumulating the ℓ_2 -norm for each block, we form the merged-energy vector ϵ to establish a one-to-one correspondence with the physical DoDs at BS (Step 3–5). The indices corresponding to the L largest elements in ϵ will form the common physical support \mathcal{I}^{BS} (Step 6). Finally, the DoDs $\{\hat{\varphi}_l\}_{l=1}^L$ can be obtained using the knowledge of \mathcal{I}^{BS} and the sampling rule of the CBS dictionary (Step 7).

Algorithm 1 DoDs Estimation at BS

Input: Angle-excluded matrix $\mathbf{x}_{k,\bar{m}}, \bar{m} \in \{1, M/2\}$, the path number L of BS-RIS channel and the quantization level of overcomplete dictionaries Q_R and Q_T .

1: $\boldsymbol{\epsilon} = [\epsilon_1, \dots, \epsilon_{Q_T}]$ and $\bar{\varphi} = -1 + \frac{1+2q}{Q_T}, \mathbf{q} = 1, \dots, Q_T$.

2: $\tilde{\boldsymbol{\epsilon}}_{\bar{m}} = \text{normalize}(|x_{k,\bar{m},1}|, \dots, |x_{k,\bar{m},Q_{\text{tot}}}|)$.

3: **for** $q \in \{1, 2, \dots, Q_T\}$ **do**

4: $\epsilon_q = \sum_{\bar{m} \in \{1, \frac{M}{2}\}} \|\tilde{\boldsymbol{\epsilon}}_{\bar{m}}(((q-1)Q_B + 1) : qQ_B)\|_2$.

5: **end for**

6: $\mathcal{I}^{\text{BS}} = \left\{ q \mid \max_k(\boldsymbol{\epsilon}, L) \right\}$

7: $\hat{\varphi} = \bar{\varphi}(\mathcal{I}^{\text{BS}})$.

Output: \mathcal{I}^{BS} and $\{\hat{\varphi}_l\}_{l=1}^L$.

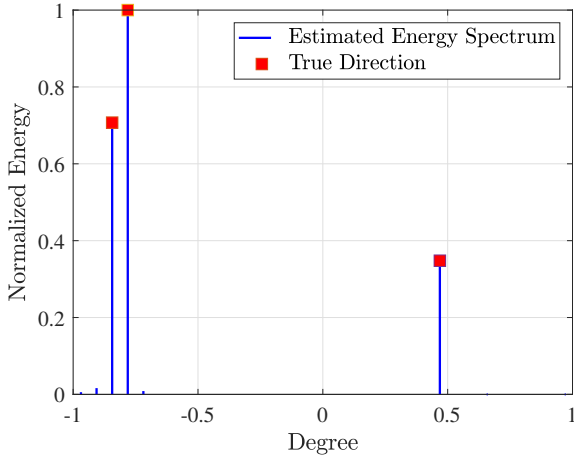


Fig. 4. Normalized energy spectrum via EnM algorithm.

Fig. 4 depicts an example of the estimated energy spectrum employing the proposed method. The cascaded channel is assumed to contain $L = 3$ BS-RIS paths with the common physical support $\mathcal{I}^{\text{BS}} = \{3, 4, 24\}$ and $\text{SNR} = 20$ dB. The spectrum reveals that the energy is distributed surrounding the estimated DoDs which closely matches the actual directions and can be easily distinguished. This validates the effectiveness of the proposed method.

2) *Common Coupled Angle Estimation at RIS:* With the estimated DoDs $\{\hat{\varphi}_l\}_{l=1}^L$, the estimated cascaded channel $\hat{\mathbf{H}}_k^{\text{cas}}[\bar{m}]$ can be projected onto the subspace of ARM of BS using the pseudo-inverse, which can be given by

$$\begin{aligned} \mathbf{U}_{k,\bar{m}} &\triangleq \hat{\mathbf{H}}_k^{\text{cas}}[\bar{m}] (\hat{\mathbf{A}}_{N_T, \bar{m}}^{\text{H}}(\boldsymbol{\varphi}))^\dagger \\ &= \text{Diag}(\mathbf{h}_k[\bar{m}]) \mathbf{A}_{R,\bar{m}}(\boldsymbol{\psi}) \boldsymbol{\Sigma}_{\bar{m}}, \end{aligned} \quad (26)$$

where $\mathbf{A}_N^\dagger \mathbf{A}_N = \mathbf{I}_L$, and $\mathbf{U}_{k,\bar{m}} \triangleq [\mathbf{u}_{k,\bar{m},1}, \dots, \mathbf{u}_{k,\bar{m},L}] \in \mathbb{C}^{N_R \times L}$ denotes the rest-CSI matrix, which is only related to the AoAs and AoDs at RIS. By substituting (7) into (26), the l -th column $\mathbf{u}_{k,\bar{m},l}$ can be expressed as

$$\begin{aligned} \mathbf{u}_{k,\bar{m},l} &= \boldsymbol{\Sigma}_{\bar{m},l} (\mathbf{A}_{R,\bar{m}}^* (\boldsymbol{\theta}_k) \boldsymbol{\beta}_{k,\bar{m}}) \bullet \mathbf{a}_{R,\bar{m}}(\boldsymbol{\psi}_l) \\ &= \boldsymbol{\Sigma}_{\bar{m},l} [\mathbf{a}_{R,\bar{m}}(\gamma_{k,l,1}), \dots, \mathbf{a}_{R,\bar{m}}(\gamma_{k,l,J_k})] \boldsymbol{\beta}_{k,\bar{m}}, \end{aligned} \quad (27)$$

where $\boldsymbol{\Sigma}_{\bar{m},l}$ denotes the (l, l) -th element in $\boldsymbol{\Sigma}_{\bar{m}}$, and $\gamma_{k,l,j} = \psi_l - \theta_{k,j} \in [-2, 2]$ represents the coupled angle for $l =$

$1, \dots, L$ and $j = 1, \dots, J_k$.

By defining $\mathbf{A}_{R,\bar{m}}(\boldsymbol{\gamma}_{k,l}) \triangleq [\mathbf{a}(\gamma_{k,l,1}), \dots, \mathbf{a}(\gamma_{k,l,J_k})] \in \mathbb{C}^{N_R \times J_k}$ as the coupled ARM, (27) can be rewritten as

$$\mathbf{u}_{k,\bar{m},l} = \mathbf{A}_{R,\bar{m}}(\boldsymbol{\gamma}_{k,l,j}) \boldsymbol{\chi}_{k,\bar{m},l}, \quad (28)$$

where $\boldsymbol{\chi}_{k,\bar{m},l} \triangleq \boldsymbol{\Sigma}_{\bar{m},l} \boldsymbol{\beta}_{k,\bar{m}} \in \mathbb{C}^{J_k}$ denotes the amplitude vector with the path gains and phase shifts for each coupled angle.

The expression in (28) represents a typical DoA estimation problem, which can be effectively addressed using the MUSIC algorithm due to its high resolution and robustness against noise [29]. However, there are two key challenges in directly applying the MUSIC algorithm. Firstly, the effective angle range for $\boldsymbol{\gamma}_{k,l,j}$, which is the difference between two angles ψ_l and $\theta_{k,j}$, is doubled compared to the classical angle range. Moreover, the relative frequency parameter η_m introduced by beam split effect further expands this range. This results in an increased number of potential estimated angles, making it difficult to distinguish the true physical directions. Secondly, the non-strict orthogonality of $\boldsymbol{\chi}_{k,\bar{m},l}$ and limited measurements at each SC can cause energy leakage into the noise space, which further complicates the identification of physical directions.

To address these challenges, we combine the information from two selected subcarriers and apply spatial smoothing preprocessing to the projected rest-CSI matrix $\mathbf{U}_{k,\bar{m}}$. Inspired by the smooth-MUSIC algorithm, we propose a novel DS-MUSIC algorithm to accurately estimate the coupled angles, as described in Algorithm 2, where $\text{maxk}(\mathbf{x}, k)$ and $\text{mink}(\mathbf{x}, k)$ return k largest peaks, k largest elements and k smallest elements of vector \mathbf{x} , respectively.

We first preprocess the projected signal $\mathbf{u}_{k,\bar{m},l}$ by dividing the RIS array into multiple overlapping subarrays, with each subarray containing N_{sub} reflecting elements. There are $N_a = N_R - N_{\text{sub}} + 1$ subarrays in total, which satisfies $N_a > N_{\text{sub}}$ and $N_a, N_{\text{sub}} > J_k$. The rest-CSI $\mathbf{u}_{k,\bar{m},l,n}$ processed by the n -th subarray can be expressed as

$$\mathbf{u}_{k,\bar{m},l,n} = \mathbf{A}_{R,\bar{m},n}(\boldsymbol{\gamma}_{k,l}) \boldsymbol{\chi}_{k,\bar{m},l}, \quad (29)$$

where $\mathbf{u}_{k,\bar{m},l,n} \triangleq \mathbf{u}_{k,\bar{m},l}(n : n + N_{\text{sub}} - 1)$ and $\mathbf{A}_{R,\bar{m},n} \triangleq \mathbf{A}_{R,\bar{m}}(:, n : n + N_{\text{sub}} - 1)$. Therefore, the covariance matrix $\mathbf{R}_{k,\bar{m},l,n}^{\text{sub}} \in \mathbb{C}^{N_{\text{sub}} \times N_{\text{sub}}}$ can be written as

$$\mathbf{R}_{k,\bar{m},l,n}^{\text{sub}} = \mathbf{u}_{k,\bar{m},l,n} \mathbf{u}_{k,\bar{m},l,n}^{\text{H}}. \quad (30)$$

To implement the spatial smoothing, the covariance matrix $\mathbf{R}_{k,\bar{m},l}^u \in \mathbb{C}^{N_{\text{sub}} \times N_{\text{sub}}}$ of $\mathbf{u}_{k,\bar{m},l}$ is calculated by averaging all N_a subarray covariance matrices $\mathbf{R}_{k,\bar{m},l,n}^{\text{sub}}$, which can be expressed by

$$\mathbf{R}_{k,\bar{m},l}^u = \frac{1}{N_a} \sum_{n=1}^{N_a} \mathbf{R}_{k,\bar{m},l,n}^{\text{sub}} = \frac{1}{N_a} \tilde{\mathbf{U}}_{k,\bar{m},l} \tilde{\mathbf{U}}_{k,\bar{m},l}^{\text{H}}, \quad (31)$$

where $\tilde{\mathbf{U}}_{k,\bar{m},l} \triangleq [\mathbf{u}_{k,\bar{m},l,1}, \dots, \mathbf{u}_{k,\bar{m},l,N_a}] \in \mathbb{C}^{N_{\text{sub}} \times N_a}$ is the concatenation of the subspace-supported vectors $\mathbf{u}_{k,\bar{m},l,n}$ as defined in (29). Then, the eigendecomposition of $\mathbf{R}_{k,\bar{m},l}^u$ can be expressed as

$$\mathbf{R}_{k,\bar{m},l}^u = \tilde{\boldsymbol{\Omega}}_{k,\bar{m},l} \text{Diag}(\tilde{\boldsymbol{\lambda}}_{k,\bar{m},l}) \tilde{\boldsymbol{\Omega}}_{k,\bar{m},l}^{\text{H}}, \quad (32)$$

Algorithm 2 DS-MUSIC Based Coupled DoAs/DoDs Estimation at RIS

Input: Projected matrix $\mathbf{U}_{k,\bar{m}}$, the path number L and J_k of the BS-RIS and RIS-UE k channel $\forall k \in \mathcal{K}$, the number of subarrays N_a and quantization level Q_R .

- 1: $\tilde{\gamma} = -2(1 + q/Q_R)$, $q = 1, \dots, Q_B$.
- 2: **for** $l \in \{1, 2, \dots, L\}$ **do**
- 3: **for** $\bar{m} \in \{1, \frac{M}{2}\}$ **do**
- 4: $\mathbf{R}_{k,\bar{m},l}^u = \frac{1}{N_a} \tilde{\mathbf{U}}_{k,\bar{m},l} \tilde{\mathbf{U}}_{k,\bar{m},l}^H$.
- 5: $[\tilde{\mathbf{\Omega}}_{k,\bar{m},l}, \tilde{\boldsymbol{\lambda}}_{k,\bar{m},l}] = \text{eig}(\mathbf{R}_{k,\bar{m},l}^u)$.
- 6: $\mathcal{S}_l = \left\{ n_\lambda \mid \min_{n_\lambda} (\tilde{\boldsymbol{\lambda}}_{k,\bar{m},l}, N_R - J_k) \right\}$.
- 7: $\mathbf{\Omega}_{k,\bar{m},l}^N = \tilde{\mathbf{\Omega}}_{k,\bar{m},l}(\mathcal{S}_l)$.
- 8: **for** $q \in \{1, 2, \dots, Q_B\}$ **do**
- 9: $\tilde{p}_q^{\text{MUSIC}} = \frac{1}{\|(\mathbf{\Omega}_{k,\bar{m},l}^N)^H \xi_{R,\bar{m},q}^{\text{sub}}\|_2^2}$.
- 10: **end for**
- 11: $\mathbf{p}_{k,\bar{m},l} = [\min(\tilde{\mathbf{p}}_{k,\bar{m},l}), \tilde{\mathbf{p}}_{k,\bar{m},l}, \min(\tilde{\mathbf{p}}_{k,\bar{m},l})]$.
- 12: $\tilde{Q}_{\bar{m},l} = \left\{ q - 1 \mid \max_k(\text{peaks}(\mathbf{p}_q), 2J_k) \right\}$.
- 13: **end for**
- 14: $\mathcal{Q}_l = \left\{ \frac{q_1 + q'_1 \frac{M}{2}}{2} \mid \min_{q_1, q'_1 \frac{M}{2}} k(d(q_1, q'_1 \frac{M}{2}), J_k) \right\}$

where $q_1 \in \tilde{Q}_{1,l}$ and $q'_1 \frac{M}{2} \in \tilde{Q}_{\frac{M}{2},l}$.

- 15: **end for**
- 16: $\mathcal{I}^{\text{RIS}} = \mathcal{Q}_1 \cup \dots \cup \mathcal{Q}_L$.
- 17: $\hat{\gamma}_k = \tilde{\gamma}(\mathcal{I}^{\text{RIS}})$.

Output: \mathcal{I}^{RIS} and $\hat{\gamma}_k$.

where $\tilde{\mathbf{\Omega}}_{k,\bar{m},l} \triangleq [\tilde{\boldsymbol{\omega}}_{k,\bar{m},l,1}, \dots, \tilde{\boldsymbol{\omega}}_{k,\bar{m},l,N_{\text{sub}}}] \in \mathbb{C}^{N_{\text{sub}} \times N_{\text{sub}}}$ denotes the eigenbasis matrix which contains N_{sub} eigenvectors and $\tilde{\boldsymbol{\lambda}}_{k,\bar{m},l} \in \mathbb{C}^{N_{\text{sub}}}$ is the eigenvalue vector. Note that $\mathbf{R}_{k,\bar{m},l}^u$ is a Hermitian matrix, which means that all its N_{sub} eigenvectors are orthogonal to each other. By arranging the eigenvalues of $\mathbf{R}_{k,\bar{m},l}^u$ in descending order and organizing the corresponding eigenvectors accordingly, it can be rewritten as

$$\mathbf{R}_{k,\bar{m},l}^u = \mathbf{\Omega}_{k,\bar{m},l} \text{Diag}(\boldsymbol{\lambda}_{k,\bar{m},l}) \mathbf{\Omega}_{k,\bar{m},l}^H, \quad (33)$$

where $\mathbf{\Omega}_{k,\bar{m},l}$ and $\boldsymbol{\lambda}_{k,\bar{m},l}$ denote the sorted eigenbasis matrix and eigenvalue vector, respectively. Therefore, the matrix $\mathbf{\Omega}_{k,\bar{m},l} \triangleq [\mathbf{\Omega}_{k,\bar{m},l}^S, \mathbf{\Omega}_{k,\bar{m},l}^N]$ can be divided into two parts: $\mathbf{\Omega}_{k,\bar{m},l}^S \in \mathbb{C}^{N_{\text{sub}} \times J_k}$ and $\mathbf{\Omega}_{k,\bar{m},l}^N \in \mathbb{C}^{N_{\text{sub}} \times (N_{\text{sub}} - J_k)}$. The part $\mathbf{\Omega}_{k,\bar{m},l}^S$ consists of the J_k largest eigenvalues corresponding to the directions of largest variability, which spans the signal subspace. The remaining $N_{\text{sub}} - J_k$ eigenvectors form $\mathbf{\Omega}_{k,\bar{m},l}^N$, spans the noise subspace and is orthogonal to the signal subspace.

To calculate the MUSIC pseudo-spectrum, the practical implementation requires sampling the estimated angles. We define $\tilde{\mathbf{p}}_{k,\bar{m},l,q} \triangleq [\tilde{p}_{k,\bar{m},l,1}, \dots, \tilde{p}_{k,\bar{m},l,Q_B}]^T$ as the MUSIC pseudo-spectrum, where $\tilde{p}_{k,\bar{m},l,q}$ is the sampling spectral value for $q = 1, \dots, Q_B$. To align these sampled values with our proposed algorithm, we adjust the angle sampling within the range of the CBS dictionary. Therefore, we define the sub-CBS dictionary $\Xi_{R,\bar{m}}^{\text{sub}} \in \mathbb{C}^{N_{\text{sub}} \times Q_B}$ as the first N_{sub} rows of

the original CBS dictionary in (15). According to (17), each element in the sub-CBS dictionary $\xi_{R,\bar{m},q}^{\text{sub}}$ can be derived as

$$\xi_{R,\bar{m},q}^{\text{sub}} \triangleq e^{-j2\pi\eta_m \left(\frac{q}{Q_R} - 1\right) \mathbf{n}_{\text{sub}}}, \quad q = 1, \dots, Q_B, \quad (34)$$

where $\mathbf{n}_{\text{sub}} = [1, \dots, N_{\text{sub}}]$.

By mapping the sampled beams $\xi_{R,\bar{m},q}^{\text{sub}}$ onto the noise space $\mathbf{\Omega}_{k,\bar{m},l}^N$, the MUSIC algorithm constructs the pseudo-spectrum by evaluating the inverse of the projection's norm at each potential direction, which can be given as

$$\tilde{p}_{k,\bar{m},l,q} = \frac{1}{\|(\mathbf{\Omega}_{k,\bar{m},l}^N)^H \xi_{R,\bar{m},q}^{\text{sub}}\|_2^2}, \quad q = 1, \dots, Q_B. \quad (35)$$

Given that any beam $\xi_{R,\bar{m},q}^{\text{sub}} \in \mathbf{\Omega}_{k,\bar{m},l}^S$ in the signal subspace should ideally have minimal projection onto the noise subspace $\mathbf{\Omega}_{k,\bar{m},l}^N$, which means that the ℓ_2 -norm in (35) associated with the actual directions should approximate zero. The MUSIC algorithm typically relies on peak detection to find actual physical directions. To avoid undetectable marginal peaks, we extend the pseudo-spectrum by inserting the minimum value at its edges. The extended pseudo-spectrum can be expressed as

$$\mathbf{p}_{k,\bar{m},l} = [\min(\tilde{\mathbf{p}}_{k,\bar{m},l}), \tilde{\mathbf{p}}_{k,\bar{m},l}, \min(\tilde{\mathbf{p}}_{k,\bar{m},l})]. \quad (36)$$

The potential directions can then be determined by employing local-maximum algorithms. However, due to the extended range of coupled angles, the estimated number of directions will be K_{cp} times the original.

Proposition 2. *The maximum number of identical beams can be given as*

$$K_{\text{cp,max}} = \lfloor \eta_m (2 - 1/Q_R) \rfloor + 1. \quad (37)$$

Proof. Recalling that the sampled beams $\xi_{R,\bar{m},q}^{\text{sub}}$ can be written as

$$\begin{aligned} \xi_{R,\bar{m},q}^{\text{sub}} &= e^{-j2\pi\eta_m \left(\frac{q}{Q_R} - 1\right) \mathbf{n}_{\text{sub}}} \\ &= e^{-j2\pi K_{\text{cp}} \mathbf{n}_{\text{sub}}} e^{-j2\pi\eta_m \left(\frac{q}{Q_R} - 1\right) \mathbf{n}_{\text{sub}}} \\ &= e^{-j2\pi\eta_m \left(\frac{q}{Q_R} - 1 + \frac{K_{\text{cp}}}{\eta_m}\right) \mathbf{n}_{\text{sub}}}, \end{aligned} \quad (38)$$

where $K_{\text{cp}} \in \mathbb{N}, \forall q = 1, \dots, Q_B$. It is observed that when $q' = q + K_{\text{cp}} Q_R / \eta_m$, the element in sub-CBS dictionary will generate the identical beam, i.e., $\xi_{R,\bar{m},q'}^{\text{sub}} = \xi_{R,\bar{m},q}^{\text{sub}}$. Therefore, the maximum number of identical beams $K_{\text{cp,max}}$ can be obtained by solving the integer equation $K_{\text{cp}} Q_R / \eta_m = Q_B$. By rearranging the terms and employing the relationship $Q_B = 2Q_R - 1$, we can obtain

$$K_{\text{cp}} = \frac{(2Q_R - 1) \eta_m}{Q_R}. \quad (39)$$

Therefore, the maximum value of K_{cp} is the integer part of this expression, which can be given as

$$K_{\text{cp,max}} = \left\lfloor \eta_m \left(2 - \frac{1}{Q_R}\right) \right\rfloor + 1. \quad (40)$$

According to Proposition 2, instead of the expected J_k peaks in the MUSIC pseudo-spectrum, $K_{\text{cp,max}} J_k$ peaks will

be detected. This makes the algorithm infeasible for distinguishing the true physical directions from fake ones within a single SC. Thankfully, it is observed from (37) that the spatial directions associated with true physical directions keep frequency-independent. Inspired by this, we propose a novel double sensing (DS) algorithm to acquire the true physical direction. In this approach, we select two SCs to calculate and compare their extended MUSIC pseudo-spectrum. The positions where peaks overlap indicate the true physical directions. However, due to the unavoidable noise and estimation errors, the pseudo-spectrum of different SCs may exist offsets. Therefore, in practical implement, we select the J_k closest peaks to represent true physical directions. We introduce the peak distance d to measure the distance between two peaks, which is given by

$$d(q_m, q'_{m'}) = |q_m - q'_{m'}|, \quad (41)$$

where q_m and $q'_{m'}$ denote the indices of the peaks at two selected SCs, respectively. So far, the detailed steps of the proposed DS-MUSIC algorithm are summarized in Algorithm 2.

To ensure the algorithm is both effective and efficient, it is crucial to select the appropriate SCs. Since $K_{cp,max}$ in (37) is affected by the choice of SCs, we should aim to satisfy $K_{cp,max} \leq 2$, which means each angle has at most two identical peaks. Employing the floor function inequality $[x] \leq x$ and substituting (5) into (37), we can obtain

$$m \leq \frac{M}{2} + \frac{M f_c Q_R}{B(Q_B)} + \frac{1}{2}. \quad (42)$$

Besides, substituting (5) into (41), the peak distance d can be derived as

$$d(q_m, q'_{m'}) = K_{cp} Q_R f_c \left| \frac{1}{f_{m'}} - \frac{1}{f_m} \right|. \quad (43)$$

To distinguish true physical directions effectively, the peak distance should also be sufficiently large. According to (43), it is evident that the intervals between selected SCs should be large enough. Therefore, under the constraint in (42), we select the first and the $M/2$ -th SCs to enhance the accuracy of estimation.

Fig. 5 depicts an example of estimated extended MUSIC pseudo-spectrum with the proposed DS approach. Assuming that the cascaded channel contains $J_k = 3$ RIS-UE paths for an arbitrary UE with SNR = 20 dB. It can be observed that the peaks overlap at actual physical directions, while those associated with fake spatial directions are completely separated. The estimated physical directions can be easily distinguished from the fake ones and accurately match the actual physical directions.

D. Channel Estimation for Other Subcarriers

Through the proposed two-step full CSI estimation, we obtained the cascaded channels for two subcarriers and the corresponding common physical angle. Based on this knowledge, the cascaded channel in (10) can be rewritten as

$$\mathbf{h}_k^{\text{cas}}[m] = (\mathbf{A}_{T,m}^*(\hat{\varphi}) \otimes \mathbf{A}_{R,m}(\hat{\gamma}_k)) \tilde{\mathbf{x}}_{k,m}, \quad (44)$$

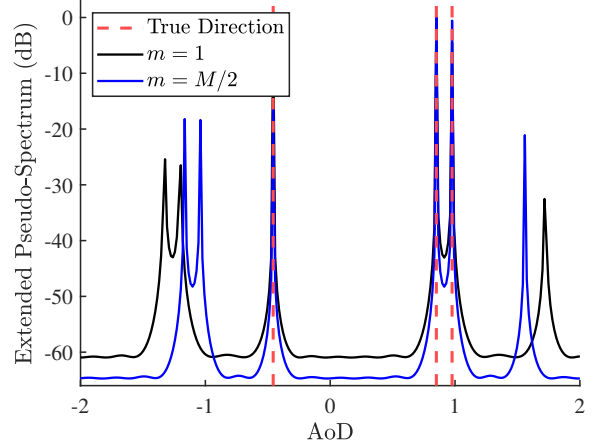


Fig. 5. Normalized extended MUSIC pseudo-spectrum via DS-MUSIC algorithm.

where $\tilde{\mathbf{x}}_{k,m} \triangleq \beta_{k,m} \otimes \boldsymbol{\Sigma}_m \in \mathbb{C}^{L^2 J_k}$ represents the angle-excluded vector, $\hat{\varphi} \triangleq [\hat{\varphi}_1, \dots, \hat{\varphi}_L] \in \mathbb{C}^L$ is the estimated DoDs at BS of all L paths, and $\hat{\gamma}_k \triangleq [\hat{\gamma}_{k,1}^T, \dots, \hat{\gamma}_{k,L}^T]^T \in \mathbb{C}^{L J_k}$ denotes the estimated coupled directions at RIS.

Substituting (44) into (20), the received signal $\mathbf{y}_{k,t}[m]$ can be rewritten as

$$\mathbf{y}_{k,t}[m] = \tilde{\Psi}_m \tilde{\mathbf{x}}_{k,m}, \quad (45)$$

where $\tilde{\Psi}_m \triangleq \bar{\mathbf{R}}_m (\mathbf{A}_{T,m}^*(\hat{\varphi}) \otimes \mathbf{A}_{R,m}(\hat{\gamma}_k)) \in \mathbb{C}^{PT \times L^2 J_k}$. The column size of the $\tilde{\Psi}_m$ matrix is reduce from $Q_B Q_T$ of overcomplete dictionary to a multipath-related size $L^2 J_k$. This significant reduction in the column size enhances both the efficiency and feasibility of the LS solution. Therefore, the angle-excluded coefficients $\tilde{\mathbf{x}}_{k,m}$ can be easily obtained as

$$\hat{\tilde{\mathbf{x}}}_{k,m} = \left(\tilde{\Psi}_m^H \tilde{\Psi}_m \right)^{-1} \tilde{\Psi}_m^H \mathbf{y}_{k,t}[m]. \quad (46)$$

Substituting (46) into (44), the full CSI for other SCs $m \in \mathcal{M} \setminus \{1, M/2\}$ can be expressed as

$$\hat{\mathbf{h}}_k^{\text{cas}}[m] = (\mathbf{A}_{T,m}^*(\hat{\varphi}) \otimes \mathbf{A}_{R,m}(\hat{\gamma}_k)) \hat{\tilde{\mathbf{x}}}_{k,m}. \quad (47)$$

IV. ANALYSIS OF COMPUTATIONAL COMPLEXITY

In this section, we analyze the computational complexity of the proposed channel estimation protocol. We also compare our results with the other existing algorithms. Specifically, the complexity of the proposed scheme mainly stems from four major components:

- 1) Cascaded channel estimation for two selected SCs by CBS-based GAMP approach: $\mathcal{O}(2PTQ_T Q_B)$.
- 2) DoDs acquisition at BS: $\mathcal{O}(Q_T Q_B)$.
- 3) Coupled directions acquisition at the RIS using DS-MUSIC algorithm: $\mathcal{O}(2N_r^3)$.
- 4) Channel estimation for other SCs: $\mathcal{O}((M-2)L^6 J_k^3)$.

The overall complexity of the proposed scheme can be expressed as

$$\mathcal{O}(2PTQ_T Q_B + 2N_r^3 + (M-2)L^6 J_k^3). \quad (48)$$

For comparison, we also discuss the complexity of the conventional OMP scheme [30], BSA-OMP scheme [17] and CBS-GAMP scheme [23]. These algorithms perform under traditional channel estimation frameworks which means they need to be executed at each SC or simultaneously process all SCs. The computational complexity of conventional OMP algorithm is $\mathcal{O}(MQ_T^3Q_R^6)$. The BSA-OMP approach has the same complexity as the conventional OMP, $\mathcal{O}(MQ_T^3Q_R^6)$, since it similarly processes each subcarrier independently. The computational complexity of CBS-GAMP is $\mathcal{O}(MPTQ_TQ_B)$. Additionally, the number of SCs M is typically large in wideband systems. Therefore, it is evident that the computational complexity of the proposed scheme is significantly lower than the other approaches mentioned.

V. NUMERICAL RESULTS AND DISCUSSION

In this section, we present numerical results to validate the effectiveness of the proposed scheme. Without loss of generality, we consider a wideband RIS-assisted THz scenario with central carrier frequency $f_c = 100$ GHz, bandwidth $B = 15$ GHz and $M = 128$ SCs. A BS employing a ULA with $N_T = 16$ antennas transmits signals to $K = 8$ single antenna UEs, with the assistance of a RIS equipped with $N_R = 64$ passive reflecting elements. For both BS-RIS and RIS-UEs channels, there exist $L = J_k = 3, \forall k$ propagation paths, and the AoAs and AoDs are randomly generated from the discretized grid within the range $[-\pi/2, \pi/2]$. The quantization level of overcomplete dictionaries is set as $Q_T = 32$ and $Q_R = 128$.

We use the normalized mean square error (NMSE) as a metric for CSI estimation performance, which is given by

$$\text{NMSE} = \mathbb{E} \left\{ \frac{\|\mathbf{h}_k^{\text{cas}}[m] - \hat{\mathbf{h}}_k^{\text{cas}}[m]\|_2^2}{\|\mathbf{h}_k^{\text{cas}}[m]\|_2^2} \right\}. \quad (49)$$

Additionally, we employ the correct probability as a metric for direction estimation performance, which is given by

$$P_c = \Pr \left\{ \left| \hat{\theta} - \theta \right| < \varepsilon_{\text{th}} \right\}, \quad (50)$$

where $\varepsilon_{\text{th}} = \delta/2$ is the threshold which is set as half the sample interval. For comparison, we also consider the conventional OMP scheme [30], BSA-OMP scheme [17], CBS-GAMP scheme [23], and oracle-LS scheme [31] as benchmark schemes in the simulation. It is noted that the angular information is assumed perfectly known in oracle-LS scheme, which can be regarded as the performance upper bound of the proposed scheme.

Fig. 6 depicts the correct probability performance of the DoDs at BS and coupled DoAs/DoDs at RIS versus SNR with $T = 50$ and $P = 30$. It is shown that both the correct probabilities approach one as SNR increases. This indicates that the proposed scheme can ensure a certain level of reliability even under low SNR conditions and has the ability to obtain accurate physical directions with sufficient channel conditions. Additionally, the correct probability of the coupled directions at RIS is consistently lower than that of the DoDs at BS across all SNR values. This is because the estimation of the coupled directions at RIS depends on the accuracy of

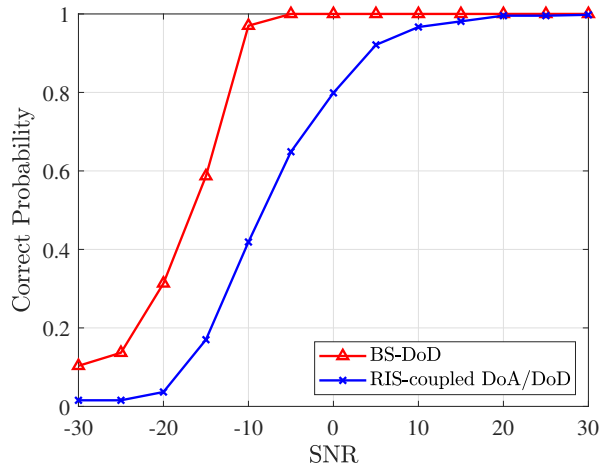


Fig. 6. Correct probability of DoDs at BS and coupled DoAs/DoDs at RIS against SNR.

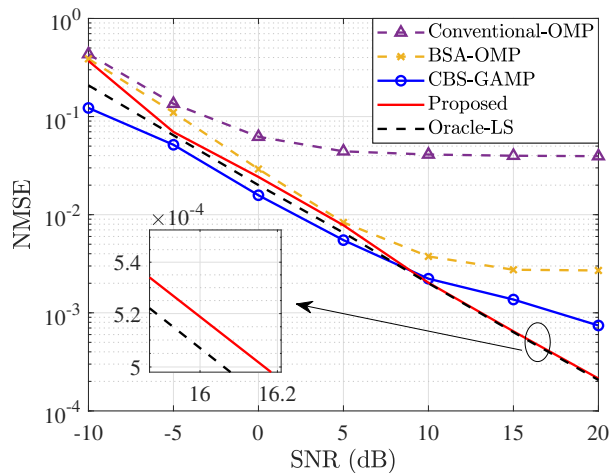
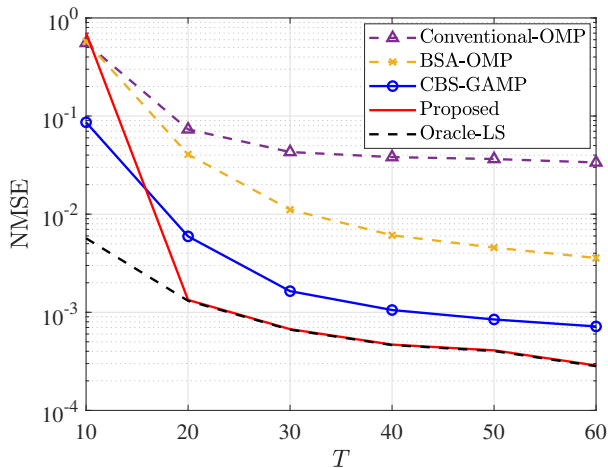
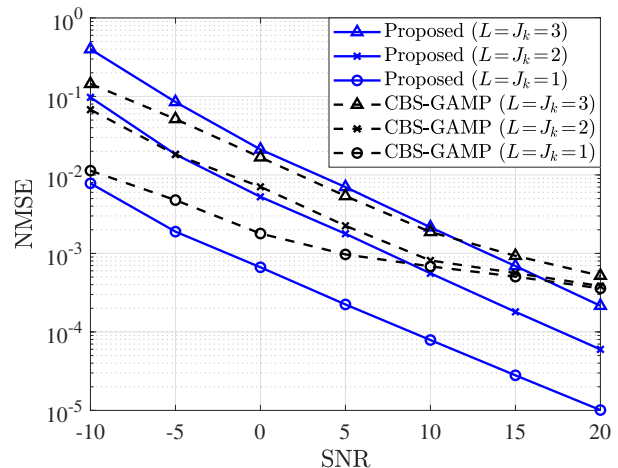
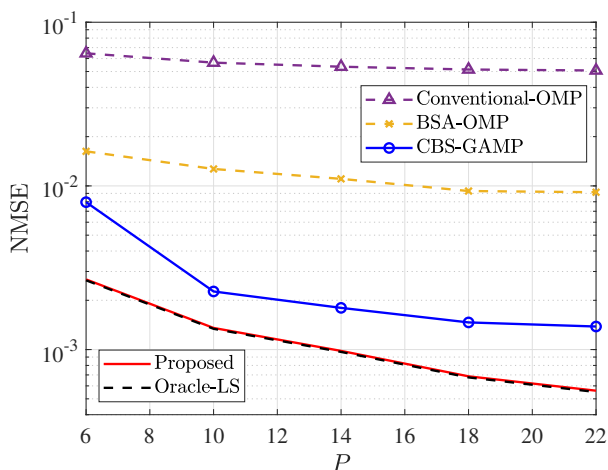
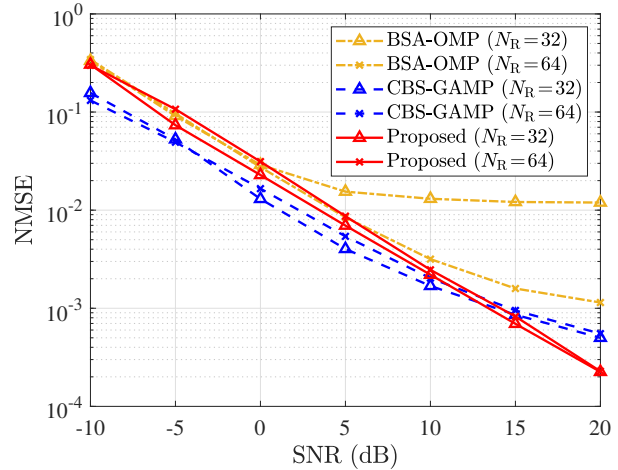


Fig. 7. NMSE performance comparison against SNR.

the DoDs estimation at BS. Angular estimation errors at BS would propagate to RIS, leading to performance gap between the two probability curves.

Fig. 7 illustrates the NMSE performance versus SNR with $T = 50$ and $P = 30$. Overall, it can be observed that the proposed scheme outperforms conventional OMP and BSA-OMP algorithm across all SNR regions. This is because the proposed scheme has the ability to exploit unknown channel information, and the proposed dictionaries can effectively cover the beam space under beam split effect. Additionally, the proposed scheme is slightly inferior to that of CBS-GAMP algorithm when SNR is less than 10 dB. This is because estimation errors generated by partial SCs propagate more significantly to the remaining SCs under poor channel conditions. However, the proposed scheme outperforms CBS-GAMP algorithm in high SNR regions, i.e., SNR is larger than 10 dB. This is because angle decoupling provides more accurate angular estimation information. This suggests that there exists a performance-complexity trade-off between these two algorithms. Moreover, it is obvious that the proposed scheme

Fig. 8. NMSE performance comparison against the number of subframes T .Fig. 10. NMSE performance comparison against the number of paths L, J_k .Fig. 9. NMSE performance comparison against the number of time slots P .Fig. 11. NMSE performance comparison against the number of reflecting elements of RIS N_R .

can approach the NMSE performance of oracle-LS scheme, which verifies the effectiveness of the proposed scheme.

Fig. 8 shows the NMSE performance versus the number of subframes T , with $\text{SNR} = 20$ dB and $P = 15$. As expected, the NMSE performance of all the algorithms improves with the increase in the number of subframes T . It can be observed that the proposed scheme maintains good performance even with a short length of subframes, e.g., $T = 10$, demonstrating the robustness of the proposed algorithm. Moreover, compared to the CBS-GAMP method, the proposed algorithm achieves similar performance with approximately a 50% subframes reduction. This indicates that the proposed scheme can efficiently reduce the pilot overhead for channel estimation.

Fig. 9 provides the NMSE performance versus the number of time slots P , with $\text{SNR} = 20$ dB and $T = 30$. As expected, the NMSE performance of all the algorithms improves with the increase in the number of slots P . It can be observed that the proposed scheme outperforms all other three algorithms and can achieve near-optimal NMSE performance of the ideal oracle-LS upper bound in all considered values of

P . The performance gap between the proposed scheme and other existing schemes is quite large. This indicates that the proposed scheme can effectively reduce the system complexity for channel estimation.

Fig. 10 illustrates the NMSE performance versus the number of paths L and J_k , with $T = 50$ and $P = 30$. It can be observed that as the the number of paths increases, the NMSE performance of both the two schemes degrade. This is because of the increased estimation parameters and challenges in distinguishing directions among more multipath components. Furthermore, as SNR increases, the NMSE of CBS-GAMP algorithm converges to around 5×10^{-4} regardless of the number of paths. In contrast, the NMSE of the proposed scheme remain decreasing across all SNR regions. This demonstrates that the proposed scheme maintains better estimation accuracy and is more robust against variations in the number of paths compared to the CBS-GAMP algorithm.

Fig. 11 shows the NMSE performance versus the number of reflecting elements of RIS N_R , with $T = 50$ and $P = 30$. It can be observed that as N_R decreases, the NMSE performance

of the BSA-OMP algorithm degrades significantly. This is because a small-scale RIS cannot provide enough measurement data diversity to support OMP based algorithms. In contrast, the performance of the proposed and CBS-GAMP schemes slightly improve as N_R decreases. This indicates that these two schemes exhibit robust framework, which are less susceptible to the lack of data diversity.

VI. CONCLUSION

In this paper, we investigated channel estimation in RIS-assisted wideband THz systems with consideration of beam split effect. We proposed a two-phase channel estimation scheme to achieve accurate CSI acquisition with reduced computational complexity. Specifically, in Phase I, we introduced a two-step method to achieve full CSI estimation over two SCs. In Phase II, we employed angular information obtained from Phase I to estimate the channels for the remaining SCs using a simple LS algorithm. Theoretical analysis and numerical results demonstrated that our scheme achieved near-oracle performance in terms of NMSE. Moreover, compared to existing solutions, the proposed two-phase strategy significantly reduced computational complexity while maintaining a high level of accuracy in CSI acquisition.

REFERENCES

- [1] H. Song and T. Nagatsuma, "Present and future of terahertz communications," *IEEE Trans. Terahertz Sci. Technol.*, vol. 1, no. 1, pp. 256–263, Sep. 2011.
- [2] P. Qin, Y. Fu, Y. Xie, K. Wu, X. Zhang, and X. Zhao, "Multi-agent learning-based optimal task offloading and UAV trajectory planning for AGIN-power IoT," *IEEE Trans. Commun.*, vol. 71, no. 7, pp. 4005–4017, May 2023.
- [3] Z. Niu, B. Zhang, Y. Zhang, Y. Feng, Z. Chen, Y. Su, Y. Fan, and Y. Guo, "Solid-state terahertz circuits and communication systems for 6G: A review," *Chinese J. Electron.*, vol. 50, no. 10, pp. 301–337, Sep. 2024.
- [4] K. Zhang, Y. Feng, Z. Xiaoyan, J. Hu, N. Xiong, S. Guo, L. Tang, and D. Liu, "Coupling enhancement of THz metamaterials source with parallel multiple beams," *Chinese J. Electron.*, vol. 32, no. 4, pp. 678–682, Sep. 2023.
- [5] Z. Chen, B. Ning, C. Han, Z. Tian, and S. Li, "Intelligent reflecting surface assisted terahertz communications toward 6G," *IEEE Wireless Commun.*, vol. 28, no. 6, pp. 110–117, Dec. 2021.
- [6] Y. Yuan, R. He, B. Ai, Z. Ma, Y. Miao, Y. Niu, J. Zhang, R. Chen, and Z. Zhong, "A 3D geometry-based THz channel model for 6G ultra massive MIMO systems," *IEEE Trans. Veh. Tech.*, vol. 71, no. 3, pp. 2251–2266, Jan. 2022.
- [7] P. Zhang, J. Zhang, H. Xiao, X. Zhang, D. W. K. Ng, and B. Ai, "Joint distributed precoding and beamforming for RIS-aided cell-free massive MIMO systems," *IEEE Trans. Veh. Tech.*, Nov. 2023.
- [8] E. Björnson, H. Wymeersch, B. Matthiesen, P. Popovski, L. Sanguinetti, and E. de Carvalho, "Reconfigurable intelligent surfaces: A signal processing perspective with wireless applications," *IEEE Signal Process. Mag.*, vol. 39, no. 2, pp. 135–158, Mar. 2022.
- [9] P. Wang, J. Fang, H. Duan, and H. Li, "Compressed channel estimation for intelligent reflecting surface-assisted millimeter wave systems," *IEEE Signal Process. Lett.*, vol. 27, pp. 905–909, May 2020.
- [10] X. Wei, D. Shen, and L. Dai, "Channel estimation for RIS assisted wireless communications—part II: An improved solution based on double-structured sparsity," *IEEE Commun. Lett.*, vol. 25, no. 5, pp. 1403–1407, May 2021.
- [11] K. Ardah, S. Gherekhloo, A. L. de Almeida, and M. Haardt, "TRICE: A channel estimation framework for RIS-aided millimeter-wave MIMO systems," *IEEE Signal Process. Lett.*, vol. 28, pp. 513–517, Feb. 2021.
- [12] G. Zhou, C. Pan, H. Ren, P. Popovski, and A. L. Swindlehurst, "Channel estimation for RIS-aided multiuser millimeter-wave systems," *IEEE Trans. Signal Process.*, vol. 70, pp. 1478–1492, Mar. 2022.
- [13] B. Ning, Z. Chen, W. Chen, Y. Du, and J. Fang, "Terahertz multi-user massive MIMO with intelligent reflecting surface: Beam training and hybrid beamforming," *IEEE Trans. Veh. Tech.*, vol. 70, no. 2, pp. 1376–1393, 2021.
- [14] M. Jian and Y. Zhao, "A modified off-grid SBL channel estimation and transmission strategy for RIS-assisted wireless communication systems," in *Proc. IEEE Int. Wireless Commun. Mobile Comput.* IEEE, Jul. 2020, pp. 1848–1853.
- [15] B. Ning, Z. Tian, W. Mei, Z. Chen, C. Han, S. Li, J. Yuan, and R. Zhang, "Beamforming technologies for ultra-massive MIMO in terahertz communications," *IEEE Open J. Commun. Soc.*, vol. 4, pp. 614–658, Feb. 2023.
- [16] J. Tan and L. Dai, "Delay-phase precoding for THz massive MIMO with beam split," in *Proc. IEEE Global Commun. Conf.* IEEE, Feb. 2019, pp. 1–6.
- [17] A. M. Elbir and S. Chatzinotas, "BSA-OMP: Beam-split-aware orthogonal matching pursuit for THz channel estimation," *IEEE Wireless Commun. Lett.*, vol. 12, no. 4, pp. 738–742, Apr. 2023.
- [18] K. Dovelos, M. Matthaiou, H. Q. Ngo, and B. Bellalta, "Channel estimation and hybrid combining for wideband terahertz massive MIMO systems," *IEEE J. Sel. Areas Commun.*, vol. 39, no. 6, pp. 1604–1620, Apr. 2021.
- [19] X. Su, R. He, B. Ai, Y. Niu, and G. Wang, "Channel estimation for RIS assisted THz systems with beam split," *IEEE Commun. Lett.*, Jan. 2024.
- [20] J. Wu, S. Kim, and B. Shim, "Parametric sparse channel estimation for RIS-assisted terahertz systems," *IEEE Trans. Commun.*, Jun. 2023.
- [21] J. Tan and L. Dai, "Wideband channel estimation for THz massive MIMO," *China Commun.*, vol. 18, no. 5, pp. 66–80, May 2021.
- [22] C. Wei, Z. Yang, J. Dang, P. Li, H. Wang, and X. Yu, "Accurate wideband channel estimation for THz massive MIMO systems," *IEEE Commun. Lett.*, vol. 27, no. 1, pp. 293–297, Jan. 2022.
- [23] X. Su, R. He, P. Zhang, and B. Ai, "Generalized approximating message passing based channel estimation for RIS-aided THz communications with beam split," *IEEE Proc. Veh. Tech. Conf.*, accepted, 2024.
- [24] H. Yang, F. Yang, S. Xu, Y. Mao, M. Li, X. Cao, and J. Gao, "A 1-bit 10×10 reconfigurable reflectarray antenna: design, optimization, and experiment," *IEEE Trans. Antennas Propag.*, vol. 64, no. 6, pp. 2246–2254, Apr. 2016.
- [25] X. Yu, D. Xu, and R. Schober, "Enabling secure wireless communications via intelligent reflecting surfaces," in *Proc. IEEE Glob. Commun. Conf.* IEEE, Dec. 2019, pp. 1–6.
- [26] D. Tse and P. Viswanath, *Fundamentals of wireless communication*. Cambridge University Press, 2005.
- [27] R. Su, L. Dai, and D. W. K. Ng, "Wideband precoding for RIS-aided THz communications," *IEEE Trans. Commun.*, Mar. 2023.
- [28] L. Dai, J. Tan, Z. Chen, and H. V. Poor, "Delay-phase precoding for wideband THz massive MIMO," *IEEE Trans. Wireless Commun.*, vol. 21, no. 9, pp. 7271–7286, Mar. 2022.
- [29] D. Kundu, "Modified MUSIC algorithm for estimating doa of signals," *Signal Process.*, vol. 48, no. 1, pp. 85–90, Dec. 1996.
- [30] J. A. Tropp and A. C. Gilbert, "Signal recovery from random measurements via orthogonal matching pursuit," *IEEE Trans. Inf. Theory*, vol. 53, no. 12, pp. 4655–4666, Dec. 2007.
- [31] H. Zou and M. Yuan, "Composite quantile regression and the oracle model selection theory," 2008.